Textural characterization of Northern Brazilian bauxites for geometallurgical modeling

Felipe Antonialli [a,b], Rafael dos Santos Macedo [a], Mauricio Guimarães Bergerman [a], Carina Ulsen [a,*]

[a] Universidade de São Paulo, Escola Politécnica - Department of Mining and Petroleum Engineering, Technological Characterization Laboratory, Brazil
[b] Mineração Rio do Norte, Brazil

A B S T R A C T

The texture of the bauxite from Porto Trombetas (Pará, Brazil) can be represented as halo (H), porcelanatic (P), grainy (G), and box-work (B) types. The influence of each texture on processing performance remains poorly understood. This work aims to evaluate whether the physicochemical properties and metallurgical behavior of bauxite are affected by bauxite texture type. Physical properties (density, porosity, moisture content, and grindability) were analyzed for 133 samples from two mines, representing the four textures. Chemical analysis was simultaneously conducted on 78 samples, to determine the major components, reactive silica, and available alumina. The samples were sub-grouped by porosity and texture. Phase-association, mineralogy and mechanical tests were examined through elemental mapping (μXRF and SEM-EDS), Rietveld refinements on X-ray diffractometry and Bond Index, respectively. The results demonstrated that porosity effectively indicates grindability and differentiates textures; whereas, drying rates are primarily controlled by reactive silica content. Deleterious minerals (mainly kaolinite) were not systematically enriched in the finer fraction (<0.037 mm). Elemental mapping provided insights into kaolinite-gibbsite interaction: in some textures, they are almost indistinguishable due to silica occlusion; whilst, in others, reactive silica is of limited significance. Texture B combines highly available alumina with low reactive silica textures. P and H exhibit pronounced weathering zones and intrinsic microporosity. G shows aluminum dilution due to the high quartz content. Microstructural analyses revealed distinct kaolinite-gibbsite associations and silica occlusion patterns. Integrating quantitative textural classification with metallurgical metrics can be a good way to perform a predictive and operationally relevant framework for optimizing beneficiation and enhancing resource utilization in tropical gibbsitic bauxites.

1. Introduction

Brazil holds one of the largest bauxite reserves in the world, estimated at approximately 2.7 billion tons. In 2024, global bauxite production reached about 450 Mt, with Brazil contributing 33 Mt, ranking fourth among producing countries, after Australia (100 Mt) [1].

Amazonian bauxite is typically gibbsitic and its deposits are commonly associated with plateaus of kilometric dimensions [2]. Despite numerous studies addressing the genesis and geochemical evolution of bauxite deposits [3,4,5,6,7,8], few have focused on differentiating the textural varieties observed within bauxitic profiles or their geometallurgical implications. Several works have described chemical parameters related to bauxitic facies [9–14], while others characterized lateritic horizons without distinguishing the internal textural variability

of the bauxitic horizon itself [8,15]. Mineralogical characterization is also well addressed in the literature, particularly regarding the evaluation of the associated crystalline phases [16].

Zainudeen et al. (2023) [17] and Anand et al. (1991) [18] presented the mineralogy and average grades of African and Australian deposits, respectively, whereas, Eggleton et al. (2009) [19] and Wang et al. (2025) [20] focused on the mineralogy of the Weipa (Australia) deposit without detailing Available Alumina (AlAP) or Reactive Silica (SiR) contents contents. Liu et al. (2023) [21] mineralogically differentiated various bauxite types from the same deposit, focusing on their genesis. Domínguez-Carretero et al. (2025) [22] and Arenque et al. (2025) [23] reported average grades for their study areas in the Dominican Republic and the Philippines, regardless of texture. Bilić et al. (2025) [24] incorporated different textures in the geochemical and mineralogical

* Corresponding author.
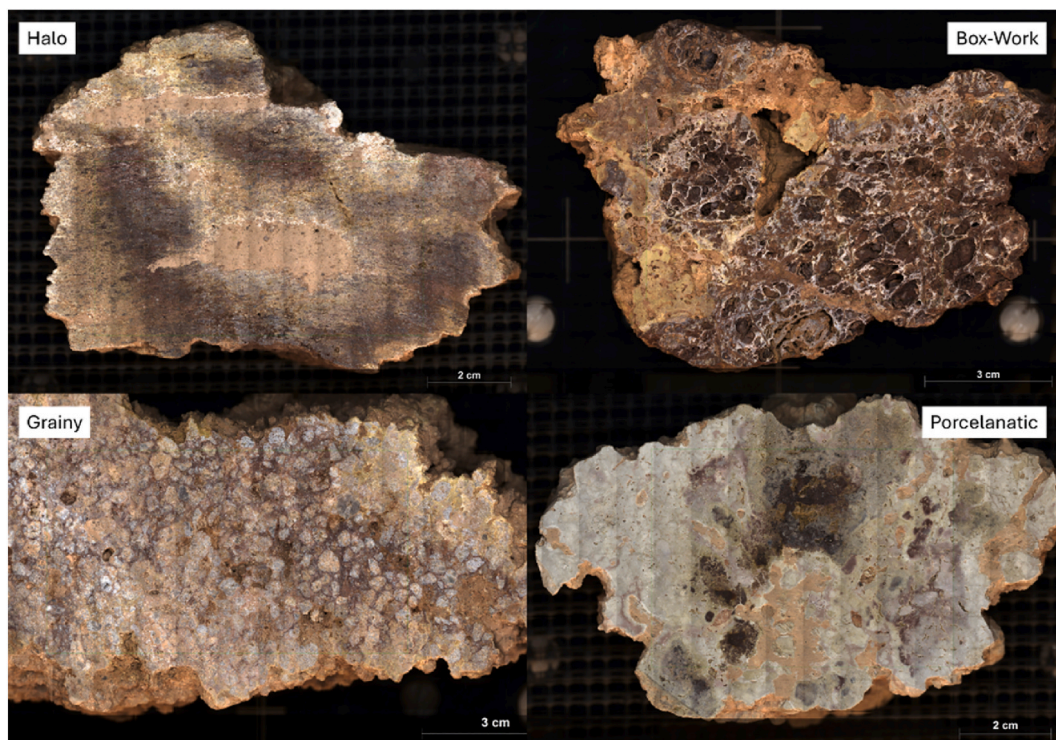E-mail address: carina.ulsen@usp.br (C. Ulsen).

Fig. 1. Bauxite textures images – Halo (H), Box-work (B), Grainy (G), Porcelanatic (P).

characterization of deposits in Bosnia and Herzegovina, and Domínguez-Carretero et al. (2025) [22] also distinguished multiple textures. Modi and Dewangan (2024) [25] demonstrated that low-grade bauxites may exhibit distinct behaviors during crushing and scrubbing, indicating the potential for process optimization and improved mineral recovery.

More recently, efforts have turned towards integrating geostatistical and predictive modeling in mineral deposits. Advanced geometallurgical modeling frameworks for bauxite mines have been proposed [11] and self-organizing maps have been applied to estimate chemical grades. Costa et al. (2024) [26] demonstrated the prediction of recoverable gold using machine learning algorithms. Studies conducted by Costa et al. (2025) [27] and Khalifani et al. (2025) performed similar work, focusing on gold and sulfides. Predictive methods, based on neural networks and using the SOM (self-organizing map) technique, were applied to bauxite and showed high effectiveness when using data from chemical analysis such as SiR and AlAP [28].

The study by Yang et al. (2024) [29] applied weights-of-evidence and machine learning methods to predict bauxite mineralization zones. Using 22,900 geochemical data points and 171 known occurrences, the authors compared logistic regression, Support Vector Machine (SVM), and Random Forest models. The Random Forest model with continuous sampling proved to be the most efficient, identifying 95.9 % of deposits within only 10 % of the area. Clay rocks and aluminum anomalies were identified as the main controlling factors. The practical application of this approach led to the discovery of the Yanfengqian deposit, containing 61.24 % Al_2O_3 and 28.95 million tons of resources. The study demonstrated that the use of machine learning significantly enhances mineral prospects in Guizhou [30]. These studies represent valuable methodological advances but still rely on bulk compositional datasets, without explicitly incorporating textural information, a factor that strongly influences beneficiation efficiency, process design, and overall resource utilization.

This body of research highlights a gap in the literature, indicating the need for integrated approaches that link texture, mineralogy, and metallurgical properties, establishing quantifiable relationships between bauxite compositions and processing performance. The present study addresses this gap through an innovative approach based on the texture-oriented geometallurgical characterization of Amazonian bauxites from the Cipó and Teófilo plateaus, i.e. from two active mines in Porto Trombetas. Four main textures: halo (H), porcelanatic (P), grainy (G) and box-work (B) were investigated to identify their intrinsic physical and compositional characteristics. Using historical drilling data combined with targeted field sampling, this work evaluates correlations between the texture and the composition of the main oxides (AlAP, SiR, and total iron (FeT)), as well as beneficiation performance (mass recovery >0.037 mm). These parameters are further related to physical (porosity, density, moisture, grindability) and mineralogical characteristics, providing an integrated assessment of bauxite behavior.

2. Materials and methods

2.1. Bauxite sample texture

The definition of the textures for characterization began with the field recognition of the dominant types, followed by the analysis and interpretation of long-term survey data to ensure broader spatial coverage. The selected textures were halo (H), porcelanatic (P), grainy (G), and box-work (B) as shown in Fig. 1.

2.2. Experimental procedure

The experimental workflow for sample selection (number of samples), processing (comminution and screening), and physical characterization (abrasion, moisture content, density, porosity, and assisted drying curve), as well as chemical (XRF), mineralogical (XRD), and microstructural analyses (SEM-EDS and μXRF), is presented in Figs. 2 and 3.

Skeletal density tests were performed using Archimedes' principle, where the skeletal volume is determined based on the water volume displaced after sample immersion in a chamber at maximum capacity. The dry mass after 12 h at 60 °C (m_{sec}) in a ventilated oven with air
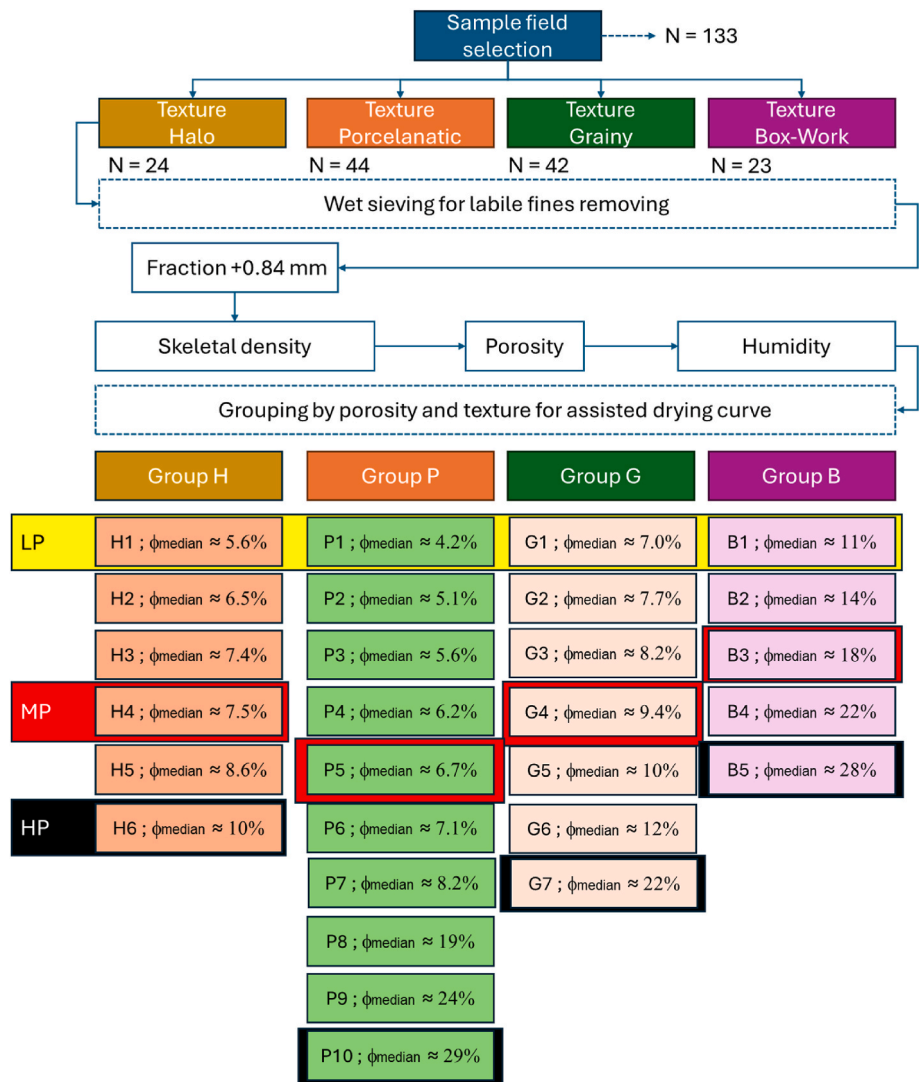
Fig. 2. Selection of samples and sub-grouping of textures at different porosities.
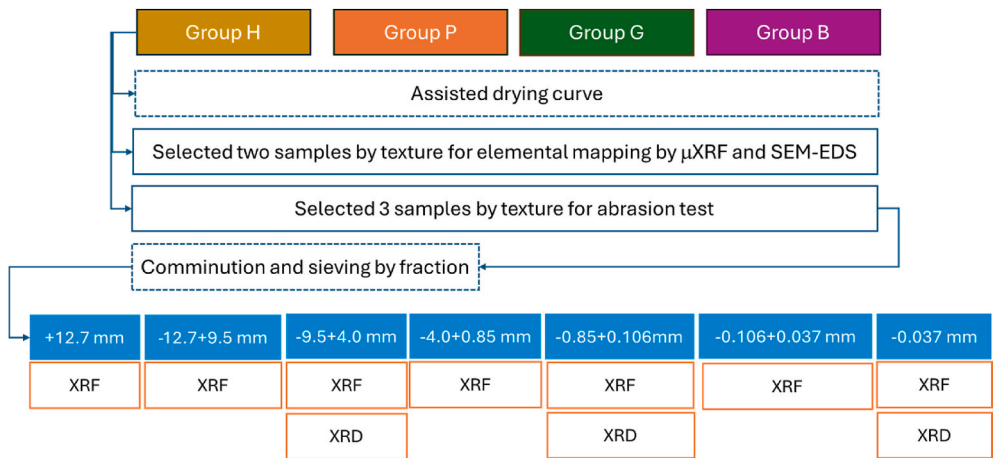

Fig. 3. Physical, microstructural, mineralogical and chemical characterization tests by porosity sub-groups.

renewal, was used for skeletal density calculations.

Porosity (ϕ) was calculated from the relationship between the saturated sample mass (m_{sat})—recorded immediately after removing the sample from immersion—and the dry mass (m_{sec}), according to Eq. (1).

$$\phi = 100*[(m_{sat} - m_{sec}) / m_{sec}] \qquad \text{Eq. (1)}$$

The porosity results were used to sub-group samples by texture and porosity. The sub-groups were numbered in ascending order of porosity.
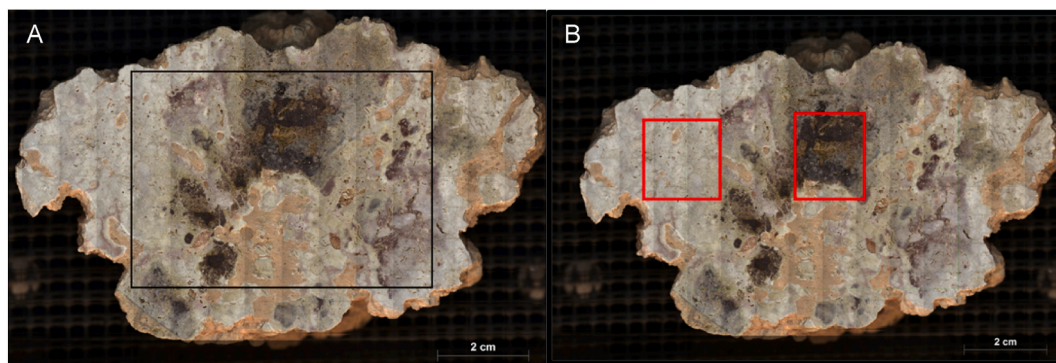
Fig. 4. Example of a sample for µXRF elemental mapping (A) and selected areas for SEM-EDS (B).

Due to significant differences in porosity among the textures, the sub-group numbers did not correspond to equivalent porosity ranges. For most textures, the last sub-groups included samples with porosities greater than 15 %, except for the halo texture. Each porosity sub-group contained 3–5 samples.

The drying kinetics were evaluated for all of the sub-groups in each texture. Samples were first immersed in water for 24 h and then placed in a static oven at 60 °C. The oven was equipped with a suspended sieve system attached to an automated dynamometer for weight readings every 3 min, as well as a high-precision thermo-hygrometer with the same acquisition interval. After 24 h, the samples were transferred to a forced-air circulation oven and dried for an additional 24 h. The data were then analyzed.

Analysis of the textures' microstructures was performed using two low-porosity samples from each texture, combining micro-X-ray fluorescence (µXRF) and scanning electron microscopy with energy-dispersive X-ray spectroscopy (SEM-EDS). Each sample was divided into three fragments, with the central portion being used for mapping, to ensure parallelism between the surfaces, as shown in Fig. 1; the remaining portions were reserved for subsequent analyses. After mapping, two regions (approximately 20 × 20 mm) per sample were selected for detailed SEM-EDS microanalysis, to refine the phase composition and microstructural understanding. This stage focused exclusively on low-porosity bauxites (LP group).

The abrasion index (Ai), ore grindability, and resistance to comminution were determined using Bond's abrasion test methodology [13]. The test was conducted in a standard Bond abrasion tester, equipped with a mild-steel paddle. The Ai was calculated as the mass loss (g) after the test. Although this method was primarily designed to determine ore abrasivity, the repeated mechanical impact also causes measurable particle breakage, allowing a qualitative assessment of ore grindability and resistance to comminution [14].

The procedure required approximately 1,600 g of sample in the 19.1–12.7 mm size fraction. Remaining fragments from the previous preparation (<19.1 mm) were crushed to obtain the required mass and particle size distribution. The product was dry sieved to assess material degradation using a mechanical shaker with the following screen apertures: 19.10, 16.00, 12.70, 9.50, 6.30, 3.35, 2.30, 1.70, 0.85, and 0.45 mm. The Bond Work Index (Wi) test was not carried out in this study; therefore, the grindability interpretations are qualitative, based on the relative resistance to breakage observed during the abrasion tests. Given its destructive nature and high mass demand, this test was conducted at the final stage of physical characterization.

Chemical analysis to determine major constituents was performed by sieved size fractions using X-ray fluorescence (XRF). Following the same preparation sequence, an aliquot was reserved for mineralogical analysis (XRD), particularly for fractions showing significant compositional variation or operational relevance.

Available alumina (AlAP) and reactive silica (SiR) contents were determined through chemical digestion, to simulate the Bayer process, which occurs by digesting a pulverized sample in a solution containing 4–7 M NaOH at temperatures ranging from 145 to 265 °C, depending on the mineralogical composition of the bauxite. Higher proportions of boehmite required higher digestion temperatures. Under these conditions, most aluminum-bearing minerals are dissolved; whereas, residual minerals such as iron oxides, quartz, and sodium aluminosilicates remain undissolved [31]. After separation of the solids and dissolved material, AlAP was determined by the titrimetric method, while SiR was quantified by flame atomic absorption spectrometry. Operational details of these methods are confidential and specific to each analytical laboratory.

2.3. Analytical techniques

Quantitative chemical analysis was carried out by XRF on fused beads prepared with anhydrous lithium tetraborate, following the quality control protocols of the analytical laboratory. Calibration curves were established from certified reference materials and used to quantify the Al_2O_3, Fe_2O_3, SiO_2, and TiO_2 content. Analyses were performed using a Malvern Panalytical Zetium spectrometer.

Mineralogical composition was determined by X-ray diffraction (XRD) using the powder method on pulverized samples, prepared by backloading method. Measurements were performed on a Malvern Panalytical Empyrean diffractometer equipped with a position-sensitive detector (PSD) and Cu Kα radiation (45 kV/40 mA). The scan covered an angular range of 2.5°–70.0° (2θ), with a step size of 0.02° and a counting time of 300 s per step. Crystalline phase identification was performed by matching diffraction patterns against the International Centre for Diffraction Data (ICDD) database.

Elemental mapping for microstructure characterization was performed on texture particles measuring 10–15 cm, as shown in Fig. 4A using µX-ray fluorescence spectrometry with an EDS detector and Rh tube (Bruker M4 Tornado), operating at 35 kV, 800 µA, 60 µm pixel resolution, and a collection time of 10 ms per pixel.

After µXRF mapping (Fig. 4A), areas of approximately 20 × 20 mm preferably those already mapped were selected for cutting and subsequent preparation for SEM-EDS analysis (Fig. 4B). Detailed chemical microanalysis mapping was conducted using a Thermo Fisher Scientific Quanta 650 FEG scanning electron microscope (SEM), equipped with Bruker XFlash 4030 and XFlash 6–60 EDS detectors. The samples had previously been embedded in resin, ground, polished, and coated with a carbon-conductive film.

3. Results and discussion

3.1. Physical characterization

A box-plot analysis of the 133 samples indicated that texture H exhibits the highest skeletal density; whereas, texture B presents the lowest. Variations in the dry-basis density of the examined textures
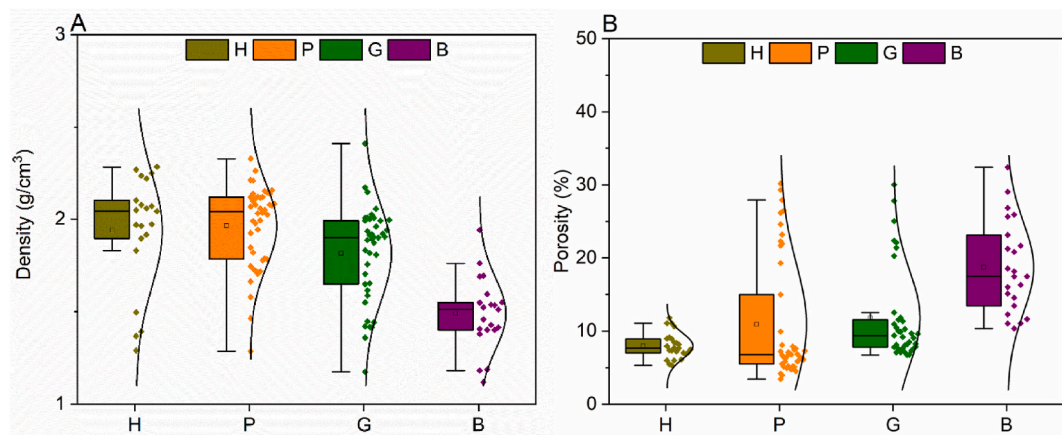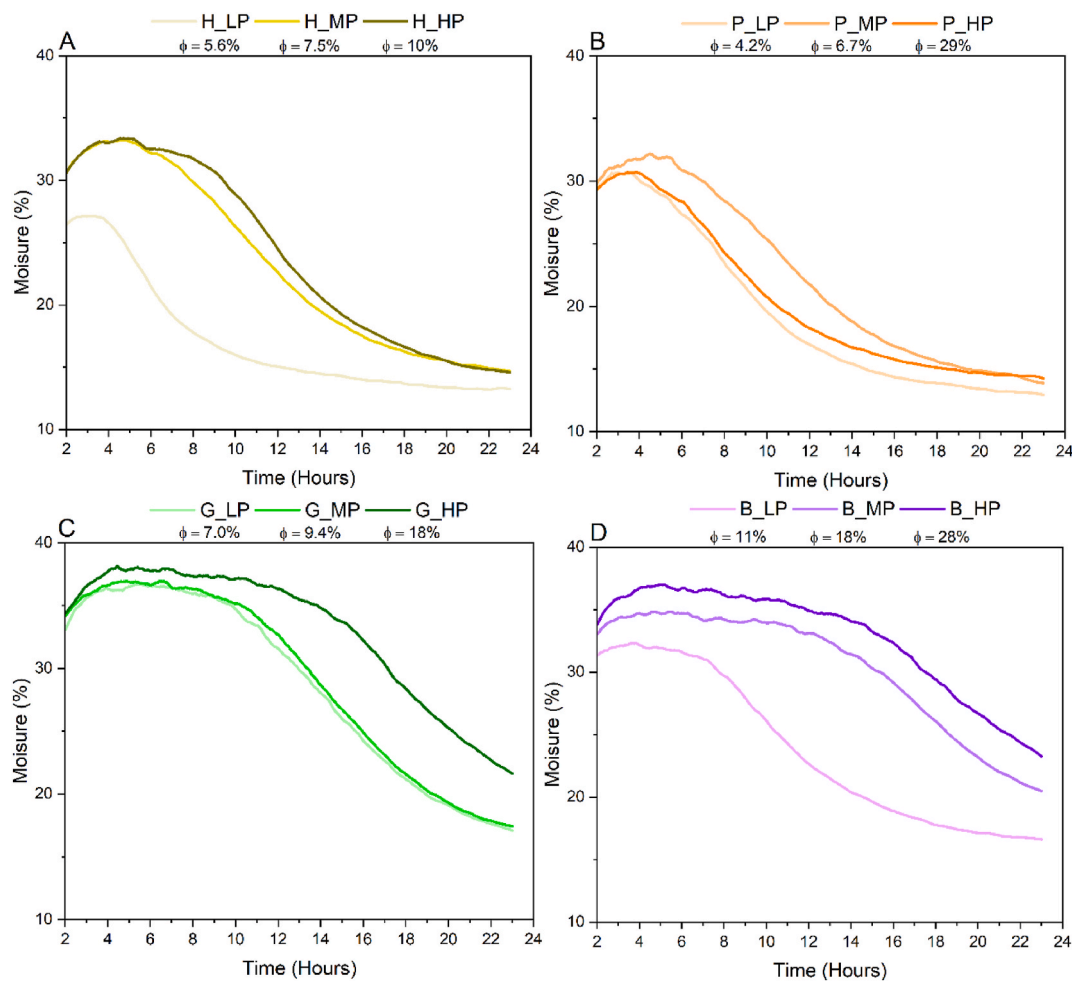
Fig. 5. (A) Density by texture and (B) estimated porosity per texture.

LP – low porosity, MP – medium porosity, HP – high porosity

Fig. 6. Drying curves by porosity and texture groups: (A) halo, (B) porcelanatic, (C) grainy and (D) box-work.

ranged from 8 to 26 % (Fig. 5A), with the largest difference occurring between textures H and B, and the smallest between textures H and P. Skeletal Density represents a relevant discriminating parameter, as it is directly associated with distinct mineralogical assemblages characterized by different intrinsic densities. The skeletal volume corresponds to the total volume of the mineralogical assembly, including the closed pores that are not accessible to water or gas [32], Archimedes' principle uses water as a mapping agent.

The studied textures displayed porosity which was inversely proportional to density, suggesting that denser textures may contain denser minerals, such as hematite. Conversely, the box-work (B) texture exhibited high porosity (Fig. 5B) and low density, possibly due to enrichment in less dense phases or the presence of confined porosity caused by trapped bubbles. The literature associates low-density
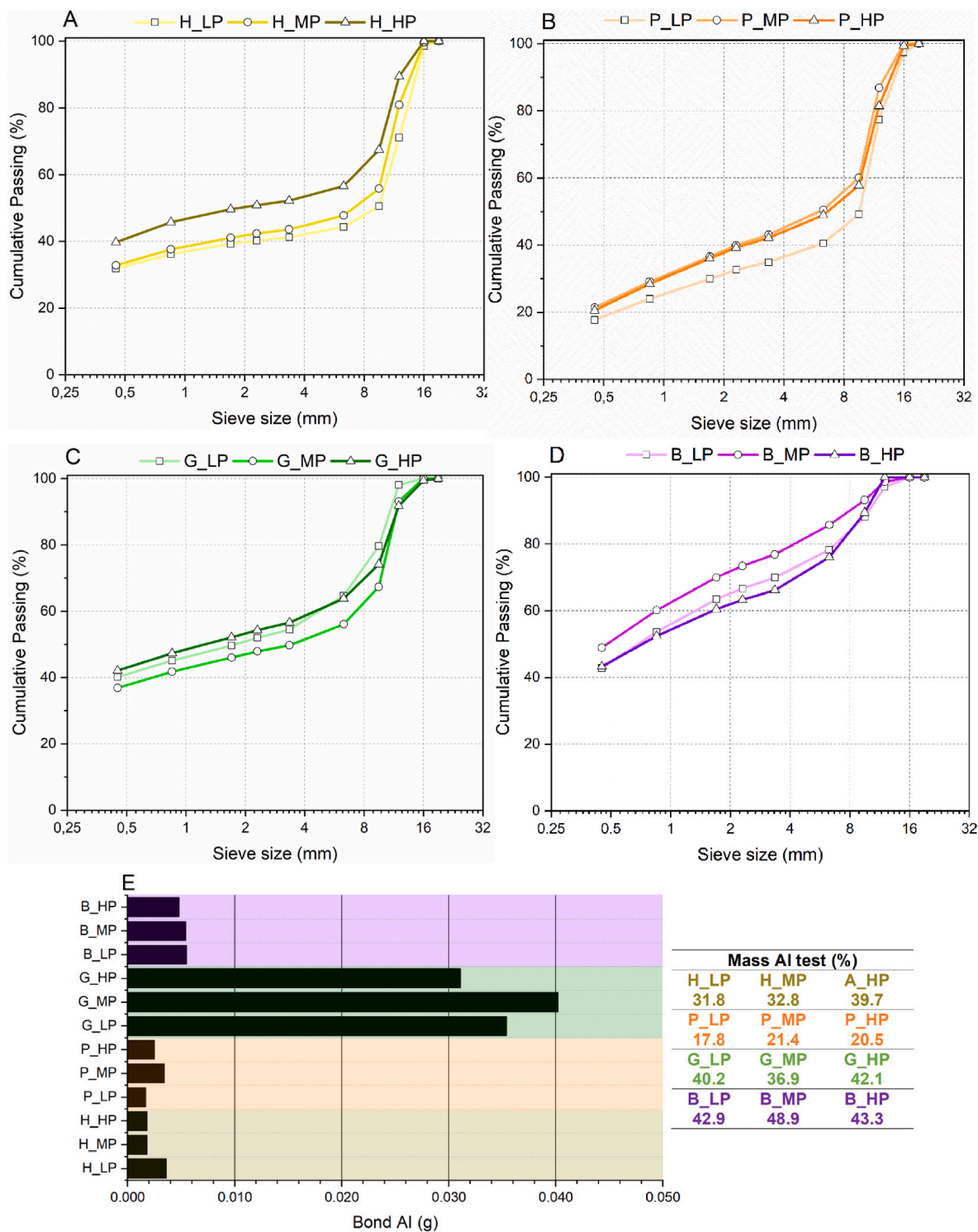
Fig. 7. Particle size distribution. Cummulative passing curve (A–D for differente textures) and mass loss below 0.45 mm with Bond AI test (E – in grams and percentage mass) per texture.

bauxites with silica dissolution and consequent increases in porosity [3, 4,15].

The P and G textures showed positive skewness with distinct porosity intervals, where the mean and median values were notably different. If only the median is considered, texture P displayed similar values to texture H. Texture B exhibited a dispersion pattern like H, with mean and median values close to each other, but its porosity values were significantly higher than those of other textures.

The similarities in porosity and density between textures H and P, or

G and B, may be associated with different weathering mechanisms or evolutionary/maturation stages of the deposit. Costa et al. (2014) [8] described the evolution of bauxites in Brazil; however, the study did not establish the evolutionary sequence of the textures, a point that still requires further regional investigation.

Porosity grouping was performed to homogenize behavior, as the observed range of porosity values warranted further sub-categorization. Samples were classified into low porosity (LP), medium porosity (MP), and high porosity (HP) groups, as illustrated in Fig. 1.

Table 1
Mineralogical composition by texture and selected fraction size.

Texture	Fraction (mm)	Minerals					
		Gibbsite	Caulinite	Hematite	Quartz	Anatase	Goethite
Halo	9,5-4,0	88	9	2	<1	1	<1
Halo	0,85-0,106	87	9	2	1	1	<1
Halo	−0.037	73	19	5	1	2	<1
Grainy	9,5-4,0	78	4	1	17	<1	<1
Grainy	0,85-0,106	66	7	1	26	<1	<1
Grainy	−0.037	71	17	5	4	1	2
Box-Work	9,5-4,0	87	5	7	<1	<1	1
Box-Work	0,85-0,106	87	3	8	<1	<1	2
Box-Work	−0.037	58	6	23	<1	2	11
Porcelanatic	9,5-4,0	83	11	5	<1	1	<1
Porcelanatic	0,85-0,106	82	13	4	<1	1	<1
Porcelanatic	−0.037	70	21	7	<1	2	<1

Fig. 8. Contents (%) of avalible Al for the different textures analyzed after sieving.
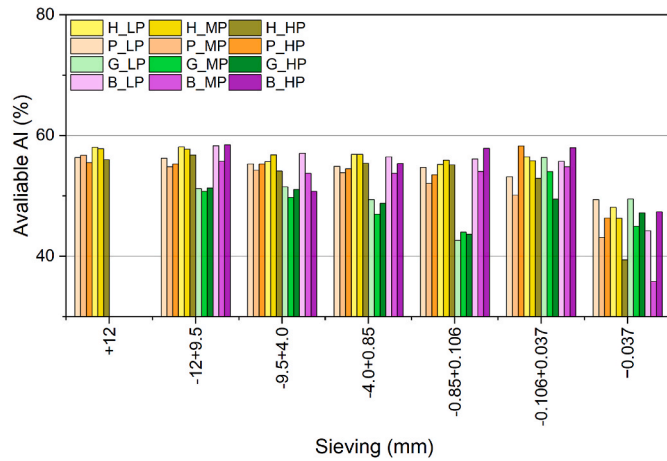

Fig. 9. Contents (%) of reactive Si for the different textures analyzed after sieving.

Assisted drying curves (Fig. 6) exhibited similar overall behavior across different porosities, although the curve shapes varied by texture. Texture P presented a defined plateau of up to 23 h for all porosities studied, presenting the smallest differences in drying times among porosity groups. Porosity had a pronounced effect on drying in texture H, particularly for low-porosity samples, which exhibited the shortest drying times. For medium and high porosity fractions of H, no significant differences were observed.

Texture G displayed consistent drying behavior across all porosity fractions, with no stabilization, even after 23 h. Similar trends were observed for texture B in medium and low porosity samples, resembling the drying behavior of high-porosity H fractions. Overall, textures with greater water retention followed the order: G > B > H > P. Water retention and drying behavior appear to be related to the geometry and connectivity of the porous network, which is consistent with the studies by Ref. [16] on pore networks in reservoir rocks.

Texture B was the most friable, indicating a higher degree of mechanical degradation under impact. In contrast, texture P generated fewer fine particles (Fig. 7A). Textures G and H displayed intermediate behavior, with cumulative curves that converged at coarser size fractions but diverged at finer ones—particularly at high porosity (H_HP)—where particle weakening became more evident. At lower porosity, the distinct separation between the curves reflects the strong textural control on fragmentation.

Texture G exhibited the highest Bond Abrasion Index (AI) (Fig. 7B), approximately one order of magnitude higher than the other textures, reflecting the presence of quartz (as evidenced in Table 1 in Section 3.2),
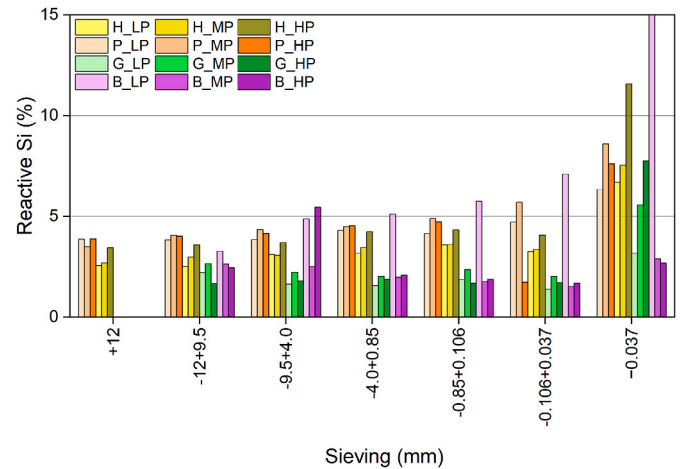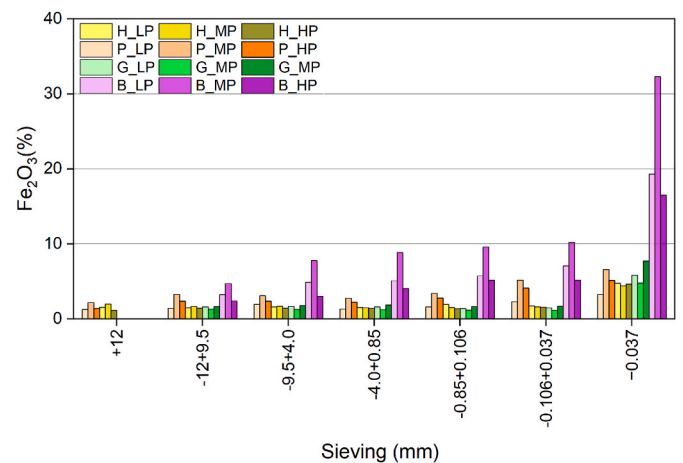

Fig. 10. Contents (%) of **Fe₂O₃** for the different textures analyzed after sieving.

which enhances abrasive wear despite the low-abrasivity classification overall [17]. Texture B, although highly friable, showed limited abrasive potential due to its fine, poorly consolidated matrix, which tends to fragment rather than abrade. In this case, abrasion is primarily associated with the elevated content of ferruginous minerals, especially hematite (as evidenced in Table 1 in Section 3.2). Therefore, all the samples were classified as low-abrasion materials according to Bond's
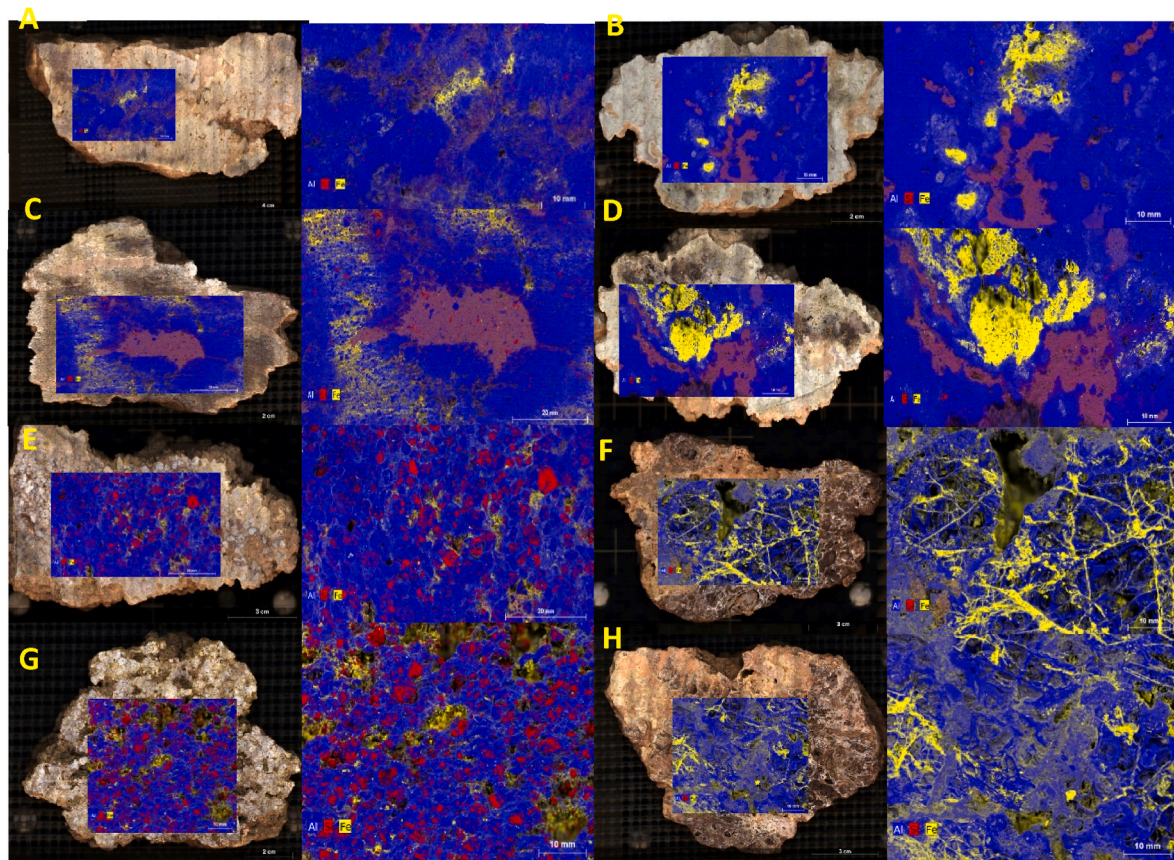
Fig. 11. μXRF by texture: where A) H_HP; B) H_LP; C) P_HP; D) P_LP; E) G_HP; F) G_LP; G) B_HP; H)B_LP. elemental maps showing Al (blue), Si (red), and Fe (yellow) distributions in representative bauxite textures.

criteria; however, the internal ranking among textures highlights distinct breakage mechanisms: friability-dominated degradation in texture B versus abrasive wear in texture G.

Due to the high friability of the low-porosity box-work samples, it was not possible to obtain the required 1,600 g for the 12–19 mm test fraction and so the test was conducted using 1,200 g. While this may have slightly underestimated the mass loss of this sample, it did not affect the relative comparisons.

3.2. Chemical and mineralogical characterization

Bauxite quality parameters are reported in terms of available aluminum (AlAP, Fig. 8), reactive silica (SiR, Fig. 9), and iron oxide content (Fig. 10). A decrease in AlAP and enrichment of SiR is observed in all of textures for particle size fractions below 0.037 mm.

The variation in grades, which was observed across the analyzed fractions, reflects the comminution behavior of each texture; i.e., not every texture maintained its chemical pattern when the original material (12 mm) was reduced in size. Regarding AlAP, textures P and H remained relatively constant across all fractions, only showing a significant decrease in the −0.037 mm fraction. Texture B exhibited a slight decrease in the intermediate fractions, while texture G showed a marked decline between the 12 mm and +0.106 mm fractions. SiR has a tendency to be concentrated in the coarser fraction (+4.00 mm) for textures G and B; whereas, textures P and H showed the opposite behavior, with SiR being concentrated in the finer fractions.

The P and H textures exhibited similar behavior, in terms of AlAP and Fe_2O_3 content, but differed regarding SiR. For fractions greater than 0.037 mm, the P texture consistently showed higher SiR values compared to H. In contrast, the H texture concentrated almost all reactive silica in fractions below 0.037 mm; whereas, in the P texture,

kaolinite was primarily associated with coarser fractions.

Despite the high porosity, low density, and elevated moisture retention observed in the drying curves, the B texture displayed the lowest reactive silica content of all the textures. This texture exhibited higher available aluminum in fractions above 0.037 mm but showed increasing Fe_2O_3 content with decreasing particle size.

Mineralogical analysis by X-ray diffraction and Rietveld quantification (Table 1). The G texture showed the lowest AlAP values in fractions greater than 0.106 mm, associated with high quartz content and low gibbsite ($Al(OH)_3$) content. In contrast, texture B maintained a high gibbsite content, even in coarser fractions, indicating that comminution is only primarily necessary if a reduction in hematite and goethite content is required.

Mineralogical analysis corroborated the chemical analysis results. Kaolinite, hematite, and goethite phases were concentrated in the fine fraction (<0.037 mm). Enrichment of kaolinite in the fine fraction was observed for the G, H, and P textures, with texture P showing the highest kaolinite content; this is consistent with the reactive silica data. Texture B exhibited low reactive silica, even in the fine fraction, similar to the chemical analysis results, and was characterized by the enrichment of Fe_2O_3, attributed to goethite ($FeO(OH)$) and hematite (Fe_2O_3).

The G texture showed the lowest AlAP values in fractions greater than 0.106 mm, associated with high quartz content and low gibbsite (Al (OH)$_3$) content. In contrast, texture B maintained a high gibbsite content, even in coarser fractions, indicating that comminution is only primarily necessary if a reduction in hematite and goethite content is required.

When comparing the textures analyzed in this study with other bauxites reported in previous works, it can be inferred that, if the oxide grades are similar, the converted AlAP and SiR grades would be lower. An example of this is Zainudeen et al. (2023) [17], who presented total
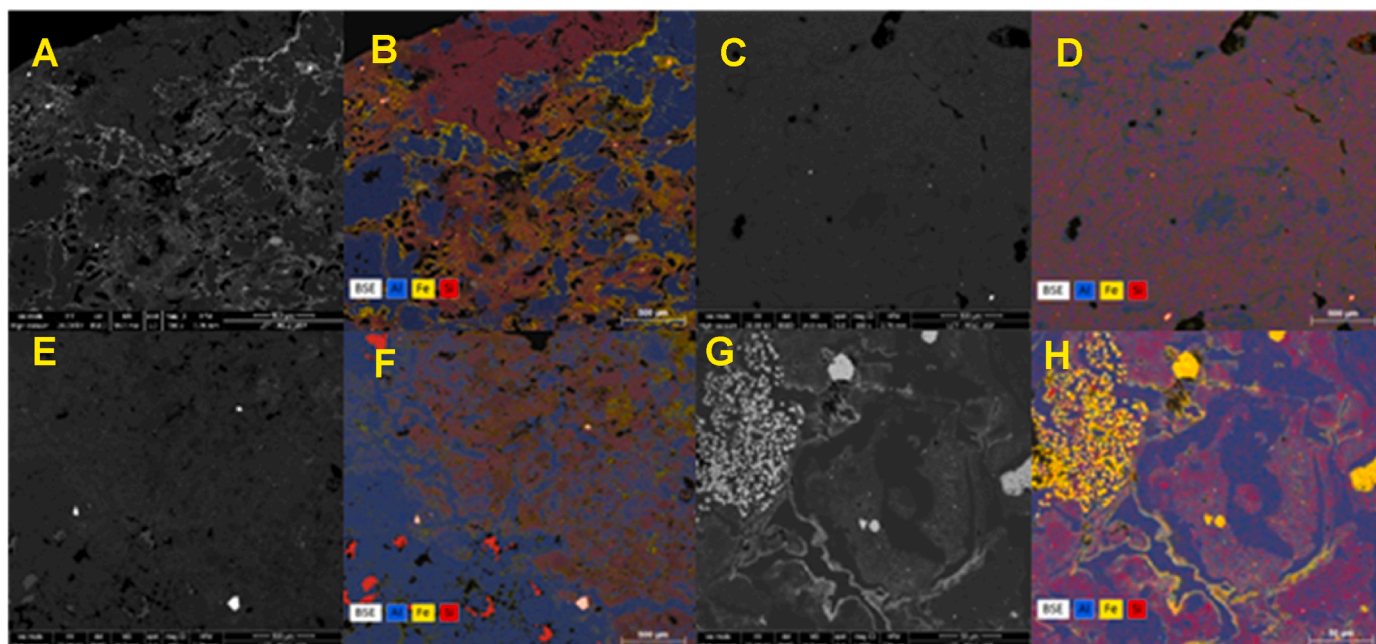
Fig. 12. SEM-EDS elemental maps showing Al (blue), Si (red), and Fe (yellow) distributions in representative bauxite textures, where (A, B) Halo high-porosity (H_HP); (C, D) Porcelanatic low-porosity (P_LP); (E, F) Grainy low-porosity (G_LP); (G, H) Box-work low-porosity (B_LP). Bright-field images (A, C, E, G) and corresponding EDS element maps (B, D, F, H) highlight compositional contrasts among the four textures.

oxide data from several mines across different African countries, unlike the present study, which reports AlAP and SiR values. Based on this premise, it is possible to state that, regardless of texture, the samples in this study consistently exhibited higher silica grades than African mines, while iron grades are only generally higher when compared with Mozambique. In contrast, overall alumina grades are higher than those of African deposits, including those from Guinea. When compared with Australian bauxites, reported by Anand et al. (1991) [18], the analyzed textures generally show higher alumina grades in all cases; whereas, iron and silica grades are lower.

In terms of mineralogy, the African bauxites described by Zainudeen et al. (2023) [17] are mainly distinguished by the presence of boehmite, a mineral not observed in any of the present samples. Meanwhile, the Australian bauxites characterized by Anand et al. (1991) [18] primarily differ due to the considerable presence of goethite; whereas, the analyzed textures include little to no goethite.

Table at SI (supplementary information) summarizes the bibliographic review used in this study, showing the mineralogy of bauxites from different mines worldwide. It can be observed that the mineralogical composition of the analyzed textures is generally similar, differing mainly in the relative abundance of each mineral phase. The absence of boehmite is a significant factor, as this aluminum-bearing mineral exhibits distinct characteristics from gibbsite, requiring higher pressures and temperatures during the Bayer process.

3.3. Microstructural characterization

The elemental mapping of texture H by μ-XRF (Fig. 11A and B) revealed reactive silica filling pores up to millimeter-sized venules. These venules radiate towards the outer regions of the ferro-aluminous nuclei, representing occluded silica-kaolinite crystals, which are closely associated with the gibbsite matrix occupying the porosity. The effect of the halo-like zones capping the ferro-aluminous portions was also observed (see Section 3.2), where the SiR grades tended to concentrate in the finer fractions, as reactive silica predominantly occurred bordering the nuclei.

In texture P (Fig. 11C and D) clayey venules occur throughout the sample. Like texture H, a halo of alteration was observed surrounding the clayey venules. The presence of these clayey venules may be the main factor contributing to SiR enrichment in the finer fractions and the maintenance of AlAP across them. This is corroborated by Fig. 7, where the mass loss due to comminution (particularly in the finer fractions) was the lowest of all the textures.

Texture G (Fig. 11E and F) comprises an aluminum-rich matrix surrounding well-defined silicon grains, probably quartz, which is consistent with the chemical analysis results for this texture.

Texture B (Fig. 11G and H) exhibited envelopes around dissolution cavities, primarily formed by ferruginous lineaments surrounded by gibbsite. The microporous cavity fillings in texture B contain lower clay mineral contents, compared with the other textures. The ferruginous films coating the aluminous matrix not only promote the retention of alumina across the fractions but, also, cause iron—removed earlier during comminution—to concentrate in the finer fractions.

SEM-EDS analyses enabled the detailed visualization of mineral associations, particularly within microporous regions, highlighting the close association of gibbsite and kaolinite (Fig. 12).

In contrast to texture H, regions near the preserved or less-altered nuclei did not exhibit alteration areolas or mineralogical gradation (gibbsite/kaolinite); however, micro-textures indicative of this mineral association were still present. Within these textures, areas less altered can be observed, which may correspond to gibbsite crystals formed during a secondary crystallization event, alongside zones with low to medium kaolinite content.

The most notable distinction in texture G, compared to the other textures, is its high content of quartz grains. In μ-XRF images, these grains are distinguishable from kaolinitic regions by their reddish coloration, uniform texture, well-defined edges, and significantly larger dimensions than kaolinite, which exhibits lighter red tones and lacks clearly defined boundaries.

In the grainy (G) texture, iron is predominantly located around the more kaolinitic areas; whereas, in the other textures, it is mainly associated with gibbsite, forming lamellae or films near pores, secondary crystals, or limiting the progression of gibbsite alteration (Fig. 12E and F).

In the grainy texture, a significant portion of the porosity occurs as spaces between mineral grains—quartz, gibbsite, and others (primary
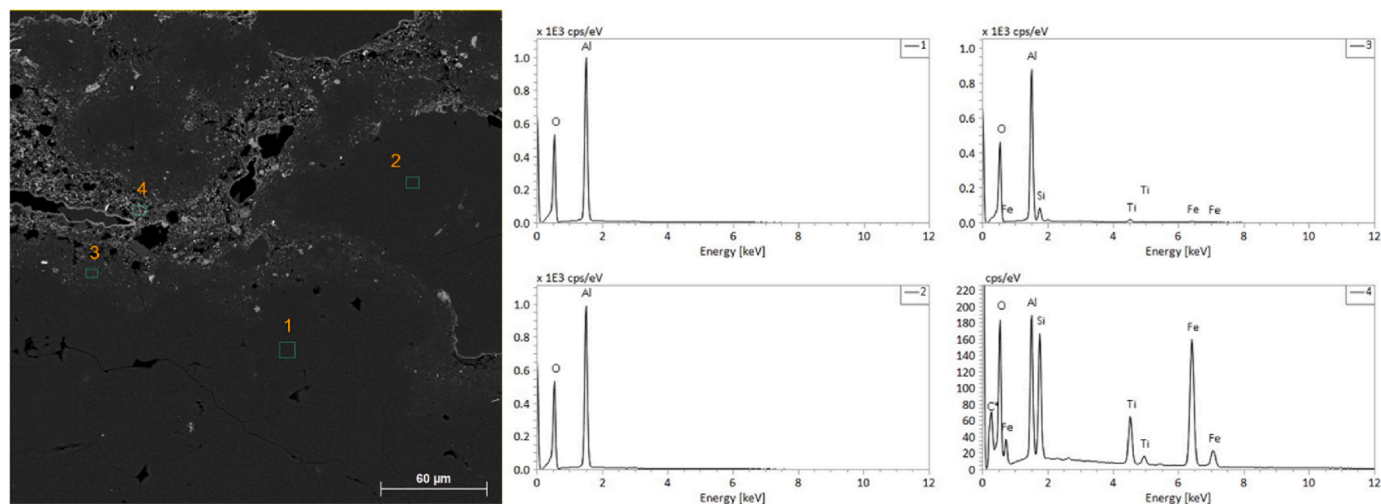
Fig. 13. SEM-EDS for sample H_HP (Φ = 10 %).
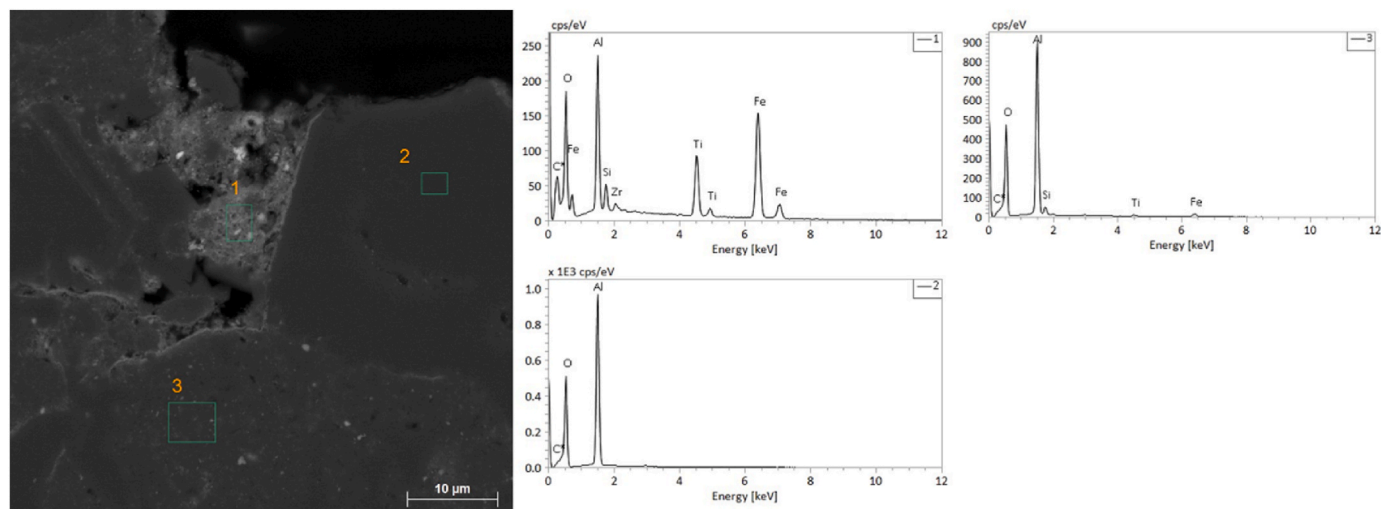
Fig. 14. SEM-EDS for sample B_LP (Φ = 11 %).
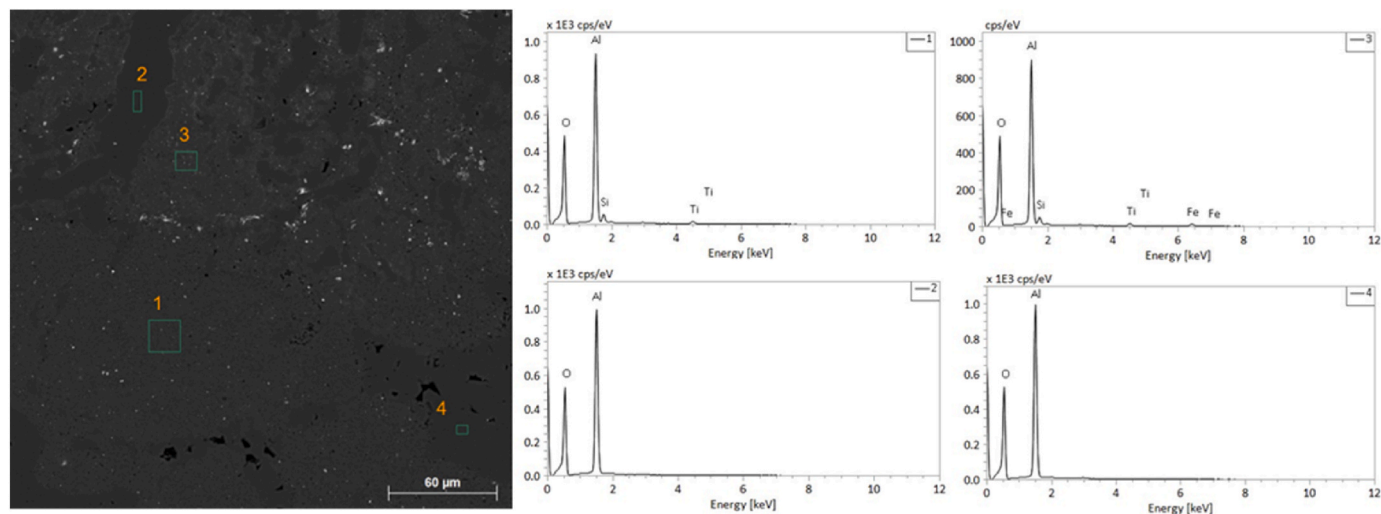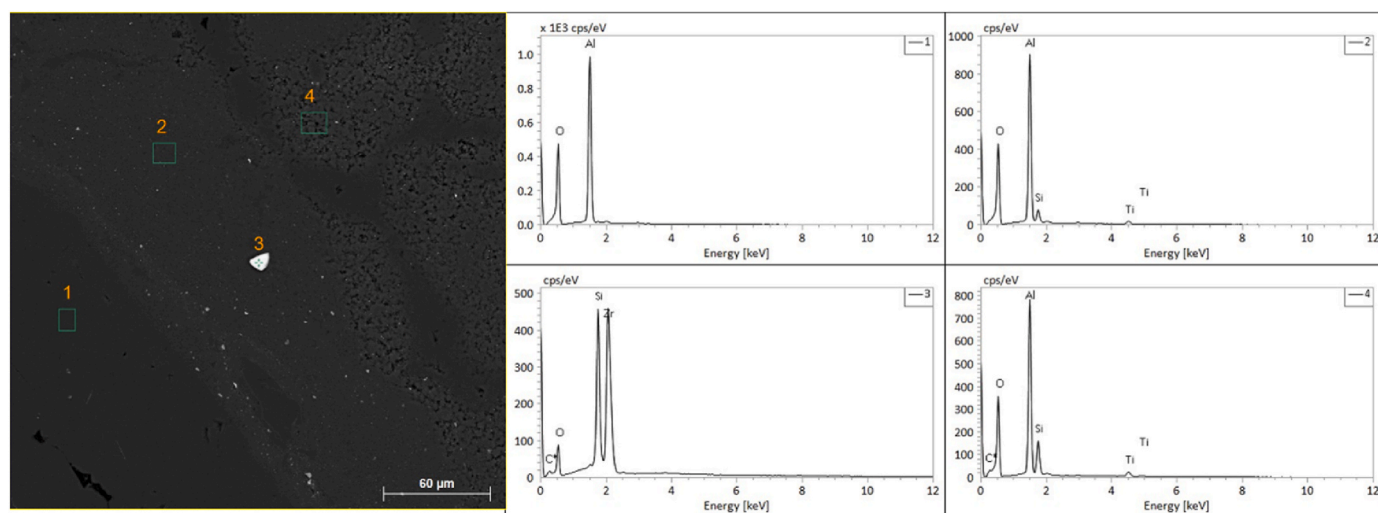

Fig. 15. SEM-EDS for sample P_LP (Φ = 4.2 %).

Fig. 16. SEM-EDS for sample G_LP (Φ = 7.0 %).

pores)—as well as secondary pores resulting from mineral dissolution, similar to other textures. These pores serve as the main points for gibbsite alteration zones.

Kaolinite is generally fine-grained and/or occluded, particularly in the more siliceous textures (halo and porcelanatic) (Fig. 12A–D). This can hinder, or even prevent, quality-enhancement procedures, such as mechanical abrasion, since not all textures benefit from roughening processes.

Ferruginous films generally act as a 'protective layer' against weathering, especially in texture B (Fig. 12F and G). Quartz crystals, in contrast to kaolinite, are concentrated in the intermediate (fine) fractions of the product. This concentration can reduce the alumina content, due to stoichiometric closure, as observed in Table 1.

The chemical microanalyses obtained by SEM-EDS, as shown in Figs. 13–16 present the chemical composition of each point, analyzed across the different textures. In Fig. 13, part of the alteration halos (typical of the halo texture) can be observed, as well as a possible second generation of gibbsite and a ferruginous lens surrounding the edges of one of the gibbsite crystals. Fig. 14 illustrates the box-work texture and indicates that the main alteration points are located near the pore edges, although they are small and of limited significance.

The porcelanatic texture (Fig. 15) exhibits a strong interaction between kaolinite and gibbsite crystals, with alteration and kaolinite-free portions being small and scattered. Moreover, altered gibbsite does not only occur near the pores but throughout the entire sample area.

The EDS analysis of the grainy texture (Fig. 16) reveals angular quartz crystals. Although generally small, the gibbsite and kaolinite crystals do not exhibit as strong an interaction as that observed in the porcelanatic texture. The grainy texture also contains preserved gibbsite crystals that remain free of kaolinite.

4. Conclusion

Bauxite textures exhibit distinct physical properties, such as density and porosity, which are not directly reflected in the available aluminum (AlAP) and reactive silica (SiR) contents. However, this apparent decoupling underscores the relevance of textural parameters as proxies for ore behavior during processing and for anticipating beneficiation challenges.

Porosity grouping proved effective in distinguishing behavioral patterns among samples, reinforcing the role of pore geometry and connectivity in controlling drying dynamics. Textures with higher porosity, such as B, exhibited lower dry density but longer drying times, while denser textures (H and P) released water more efficiently. These

variations demonstrate that porosity and pore network architecture governs drying performance.

Texture-specific contrasts were evident. Despite its high porosity, texture B displayed low SiR and high AlAP, indicating a favorable chemical profile with fewer beneficiation steps being required to remove contaminants. This reduced processing demand minimizes particle degradation and the loss of fines during classification. In contrast, textures P and H show the stronger development of resistant mineral phases and higher proportions of alumino-silicates, requiring more intensive de-sliming and attrition to lower reactive silica, which can increase degradation and operational costs. The G texture, however, shows aluminum dilution due to its high quartz content—an inert phase under Bayer digestion but one that contributes to greater residue generation and lower alumina yield.

Microstructural analyses, integrating image analysis with chemical signatures at multiple scales, enabled the identification and spatial discrimination of weathering zones. Texture P reveals a strong intrinsic association between aluminum and aluminosilicates, supporting the interpretation of progressive silica fixation during lateritic alteration.

Collectively, these findings reinforce the fact that textural heterogeneity plays a decisive role in ore performance. They emphasize the importance of texture-driven strategies to enhance bauxite beneficiation efficiency, minimize reactive silica penalties, and reduce operational costs, while offering a framework for predictive classification and process adjustment in future industrial applications.

Declaration of competing interest

The authors declare that they have no known competing financial interests or personal relationships that could have appeared to influence the work reported in this paper.

Appendix A. Supplementary data

Supplementary data to this article can be found online at https://doi.org/10.1016/j.jmrt.2025.12.012.

References

[1] UNITED STATES GEOLOGICAL SURVEY. Mineral commodity summaries 2025. 2025. https://doi.org/10.3133/mcs2025.

[2] Costa ML da, Cruz G da S, Almeida HDF de, Poellmann H. On the geology, mineralogy and geochemistry of the bauxite-bearing regolith in the lower Amazon basin: evidence of genetic relationships. J Geochemical Explor 2014;146:58–74. https://doi.org/10.1016/j.gexplo.2014.07.021.

[3] Modi M, Dewangan P. Beneficiation of Bauxite ore characterized by low-grade and High Silica Content using crushing and scrubbing technique. Int J Eng Trends Technol 2024;72:207–13. https://doi.org/10.14445/22315381/IJETT-V72I7P122.

[4] Liu L, Liu X, Yang S, Zhao L, Sun X, Zhang J. Mineralogical and geochemical investigations on the early Permian Yuxi karstic bauxite deposit, Central Yunnan, China. Ore Geol Rev 2023;153:105296. https://doi.org/10.1016/j.oregeorev.2023.105296.

[5] Arenque LA, Gabo-Ratio JA, Payot BD, Guzman JT, Yonezu K. Mineralogy and geochemistry of the Paranas karst bauxite deposit of Samar Island, Philippines. IOP Conf Ser Earth Environ Sci 2025;1517:012040. https://doi.org/10.1088/1755-1315/1517/1/012040.

[6] Bilić Š, Peytcheva I, Georgiev S, Holma M, Hikov A, Pavičić I, et al. Mineralogy, petrology, geochemistry and U-Pb zircon age of Upper Cretaceous bauxites from Jajce, Bosnia and Herzegovina. Ore Geol Rev 2025;184:106736. https://doi.org/10.1016/j.oregeorev.2025.106736.

[7] Silva FANG, Sampaio JA, Garrido FMS, Medeiros ME. Study on the characterization of marginal bauxite from Pará/Brazil. In: Light met. 2011. Cham: Springer International Publishing; 2011. p. 13–8. https://doi.org/10.1007/978-3-319-48160-9_2.

[8] Costa ML da, Cruz G da S, Almeida HDF de, Poellmann H. On the geology, mineralogy and geochemistry of the bauxite-bearing regolith in the lower Amazon basin: evidence of genetic relationships. J Geochemical Explor 2014;146:58–74. https://doi.org/10.1016/j.gexplo.2014.07.021.

[9] Mathieu MN, Paul T, Martin Y. Multi-Scale Organization of the Doumbouo-Fokoué Bauxites Ore Deposits (West Cameroon): implication to the Landscape Lowering. Open J Geol 2012;2:14–24. https://doi.org/10.4236/ojg.2012.21002.

[10] Boulangé B, Carvalho A. The bauxite of Porto de Trombetas. Brazilian Bauxites 1997:107–33.

[11] Mondillo N, Di Nuzzo M, Kalaitzidis S, Boni M, Santoro L, Balassone G. Petrographic and geochemical features of the B3 bauxite horizon (Cenomanian-Turonian) in the Parnassos-Ghiona area: a contribution towards the genesis of the Greek karst bauxites. Ore Geol Rev 2022;143:104759. https://doi.org/10.1016/j.oregeorev.2022.104759.

[12] Miranda D, Santos C, Santos F, Meneses A, Clemente CM, Oliveira R, et al. The bauxite-bearing lateritic profile of the Jequié Complex, São Francisco Craton, Brazil: potential for rare earth elements mineralization and insights on the mineral system. J Geol Surv Brazil 2023;6:165–91. https://doi.org/10.29396/jgsb.2023.v6.n2.2.

[13] Negrão LBA, Costa ML da. Mineralogy and geochemistry of a bauxite-bearing lateritic profile supporting the identification of its parent rocks in the domain of the huge Carajás iron deposits, Brazil. J South Am Earth Sci 2021;108. https://doi.org/10.1016/j.jsames.2021.103164.

[14] Silva FANG, Sampaio JA, Garrido FMS, Medeiros ME. Study on the characterization of marginal bauxite from Pará/Brazil. In: Light met. 2011. Cham: Springer International Publishing; 2011. p. 13–8. https://doi.org/10.1007/978-3-319-48160-9_2.

[15] da Rocha Pereira B, Rosset M, de Oliveria Lima JD, Gomes KP, Espinosa DCR, Tenório JAS. Characterization Study of some bauxite deposits in Northern Brazil. Clays Clay Miner 2023;71:707–21. https://doi.org/10.1007/s42860-023-00264-2.

[16] Melo CCA, Angélica RS, Paz SPA. A method for quality control of bauxites: case study of brazilian bauxites using plsr on transmission xrd data. Minerals 2021;11:1–12. https://doi.org/10.3390/min11101054.

[17] Zainudeen NM, Mohammed L, Nyamful A, Adotey D, Osae SK. A comparative review of the mineralogical and chemical composition of African major bauxite deposits. Heliyon 2023;9:e19070. https://doi.org/10.1016/j.heliyon.2023.e19070.

[18] Anand RR, Gilkes RJ, Roach GID. Geochemical and mineralogical characteristics of bauxites, Darling Range, Western Australia. Appl Geochem 1991;6:233–48. https://doi.org/10.1016/0883-2927(91)90001-6.

[19] Eggleton RA, Taylor G, Gleuher M Le, Tilley DB, Taylor G, et al. Regolith profile , mineralogy and geochemistry of the Weipa Bauxite , northern Australia Weipa Bauxite , northern Australia 2009;0099. https://doi.org/10.1080/08120090802438233.

[20] Wang Y, Liu W, Liu W, Chen M. Synergistic regulation of critical metal ions lattice substitution mechanisms on flotation separation and leaching behaviour of bauxite : experiments and DFT calculations, vol. 231; 2025.

[21] Liu L, Liu X, Yang S, Zhao L, Sun X, Zhang J. Mineralogical and geochemical investigations on the early Permian Yuxi karstic bauxite deposit, Central Yunnan, China. Ore Geol Rev 2023;153:105296. https://doi.org/10.1016/j.oregeorev.2023.105296.

[22] Domínguez-Carretero D, Villanova-de-Benavent C, Torró L, Pujol-Solà N, Bover-Arnal T, Mestre À, et al. Mineralogy , geochemistry and origin of karst bauxite deposits from the Reserva Fiscal Ávila , SW Dominican Republic. Geol Acta 2025;23:1–18. https://doi.org/10.1344/GeologicaActa2025.23.9.

[23] Arenque LA, Gabo-Ratio JA, Payot BD, Guzman JT, Yonezu K. Mineralogy and geochemistry of the Paranas karst bauxite deposit of Samar Island, Philippines. IOP Conf Ser Earth Environ Sci 2025;1517:012040. https://doi.org/10.1088/1755-1315/1517/1/012040.

[24] Bilić Š, Peytcheva I, Georgiev S, Holma M, Hikov A, Pavičić I, et al. Mineralogy, petrology, geochemistry and U-Pb zircon age of Upper Cretaceous bauxites from Jajce, Bosnia and Herzegovina. Ore Geol Rev 2025;184:106736. https://doi.org/10.1016/j.oregeorev.2025.106736.

[25] Modi M, Dewangan P. Beneficiation of Bauxite ore characterized by low-grade and High Silica Content using crushing and scrubbing technique. Int J Eng Trends Technol 2024;72:207–13. https://doi.org/10.14445/22315381/IJETT-V72I7P122.

[26] Costa FR, de Carvalho Carneiro C, Ulsen C. Predicting gold accessibility from mineralogical characterization using machine learning algorithms. J Mater Res Technol 2024;29:668–77. https://doi.org/10.1016/j.jmrt.2024.01.139.

[27] Costa FR, Carneiro C de C, Ulsen C. Enhanced gold ore classification: a comparative analysis of machine learning techniques with textural and chemical data. Geosciences 2025;15:248. https://doi.org/10.3390/geosciences15070248.

[28] de Carvalho Carneiro C, Del Valle Silva Yanez DN, Ulsen C, Fraser SJ, Antoniassi JL, Paz SPA, et al. Imputation of reactive silica and available alumina in bauxites by self-organizing maps. 2017 12th Int. Work. Self-Organizing Maps Learn. Vector Quantization, Clust. Data Vis. IEEE 2017:1–6. https://doi.org/10.1109/WSOM.2017.8020008.

[29] Yang S, Yang W, Cui T, Zhang M. Prediction and practical application of bauxite mineralization in Wuzhengdao area, Guizhou, China. PLoS One 2024;19:e0305917. https://doi.org/10.1371/journal.pone.0305917.

[30] Yang S, Yang W, Cui T, Zhang M. Prediction and practical application of bauxite mineralization in Wuzhengdao area, Guizhou, China. PLoS One 2024;19:e0305917. https://doi.org/10.1371/journal.pone.0305917.

[31] Hind AR, Bhargava SK, Grocott SC. The surface chemistry of Bayer process solids: a review. Colloids Surfaces A Physicochem Eng Asp 1999;146:359–74. https://doi.org/10.1016/S0927-7757(98)00798-5.

[32] Park S, Kang M-C, Oinam Y, Amoozegar A, Pyo S. Measurement of skeletal density and porosity of construction materials using a new proposed vacuum pycnometer. Measurement 2022;196:111209. https://doi.org/10.1016/j.measurement.2022.111209.